

Quantifying the transition of impact mechanisms of geophysical flows against flexible barrier

Yong Kong^a, Xingyue Li^b, Jidong Zhao^{a,*}

^a Department of Civil and Environmental Engineering, The Hong Kong University of Science and Technology, Clear Water Bay, Hong Kong SAR, China

^b School of Architecture, Civil and Environmental Engineering, Swiss Federal Institute of Technology, Lausanne, Switzerland

ARTICLE INFO

Keywords:

Geophysical flows
Flexible barrier
Impact mechanism transition
Runup
Pile-up
CFD-DEM

ABSTRACT

Flexible barriers have been increasingly used worldwide for mitigating natural hazards involving various geophysical flows. The analysis and design of flexible barriers need to distinguish two major impact mechanisms, runup and pile-up, which remain poorly understood due to complicated interactions between the impacting flow and the deformable barrier. In this study, a unified computational approach based on coupled computational fluid dynamics and discrete element method (CFD-DEM) is employed to examine the impact mechanisms of a wide spectrum of geophysical flows against a deformable and permeable flexible barrier. We consider geophysical flows including rock avalanche, debris avalanche, debris flow, debris flood and mud flow, and a flexible barrier consisting of a barrier net, cables and brakes. The signatures of runup and pile-up mechanisms are thoroughly analyzed, in terms of flow features and barrier responses. The effects of Froude numbers ($Fr = 0.46\text{--}7.40$), solid volume concentrations ($0.1\text{--}1$), and fluid rheologies (Newtonian and non-Newtonian fluids) on the impact mechanism transitions are systematically examined. Two nondimensional indices, the static-peak load ratio of the barrier and the momentum reduction ratio of the flow, are proposed for identifying the transition of impact mechanism from pile-up to runup. The transition is found to occur with either an increase in Fr or solid volume concentration of the flow. Increased viscosity of the fluid in a solid-fluid mixture may result in a transition occurring at a higher Fr . This study helps gain insights into the two impact mechanisms and their transitions and may provide a useful reference for the future design of flexible barriers in mitigating hazardous geophysical flows.

1. Introduction

Geophysical flows are among the most destructive natural hazards that cause heavy casualties and significant damages to key infrastructures worldwide every year. The ever-growing climate change and extreme weather events have contributed to the increase in the frequency, duration and intensity of these catastrophic flows (Guerreiro et al., 2018). In practical combats of natural hazards, flexible barriers have been increasingly used for intercepting a wide spectrum of geophysical flows (Geobruigg, 2012; Wendeler et al., 2019), ranging from rock avalanche and debris avalanche to debris flow, debris flood and mud flow (see Table 1), to mitigate their hazardous impacts. Compared to rigid mitigation measures (Hu et al., 2020; Su et al., 2021), flexible barriers are easy and economical to be installed, maintained and replaced, especially in mountainous regions. They may also offer visually non-intrusive options for geophysical flow mitigation in hilly urban

areas. The design of a safe flexible barrier system to resist geophysical flows, however, remains empirically based approaches that are predominantly modified from rigid barrier designs. The major challenges root in poor understandings of the dynamic interacting mechanisms between a permeable flexible barrier and a multiphase geophysical flow (Pudasaini and Mergili, 2019) that frequently involve complicated multi-scale, multi-phase, multi-body, and multi-way interactions during a typical impacting process (Figs. 1a and c). Except for limited small-scale experiments, there are no analytical tools that enable systematic investigations of such processes to provide theoretical bases for relevant design.

The impact behavior of geophysical flows against resisting barriers has been found governed by two main mechanisms: runup and pile-up (e.g. Ashwood and Hungr, 2016; Kattel et al., 2018; Liu et al., 2020a; Song et al., 2017). Observations based on experimental and field impact tests of flows on permeable flexible barriers (e.g. Geobruigg, 2012;

* Corresponding author.

E-mail addresses: ykongad@connect.ust.hk (Y. Kong), xingyue.li@epfl.ch (X. Li), jzhao@ust.hk (J. Zhao).

<https://doi.org/10.1016/j.enggeo.2021.106188>

Received 8 December 2020; Received in revised form 3 May 2021; Accepted 6 May 2021

Available online 8 May 2021

0013-7952/© 2021 Elsevier B.V. All rights reserved.

Table 1

Classification of rapid geophysical flows (modified from Coussot and Meunier, 1996; Hungr et al., 2001).

Name	Solid material	Fluid content	Velocity
Rock avalanche	Fragmented rock	Varied, mainly dry	Extremely rapid
Debris avalanche	Debris	Partly or fully saturated	Extremely rapid
Debris flood	Debris	Free water present	Extremely rapid
Debris flow	Debris, increased fine solids	Saturated	Extremely rapid
Mud flow	Fine, cohesive materials	At or above the liquid limit	Rapid

(HKUST, 2019) suggest the schematic vertical cross-sections of the two mechanisms as illustrated in Figs. 1b and d, respectively. Either of the impact mechanisms is preceded by a frontal impact process as shown in Stage I in Fig. 1 when a geophysical flow first impacts a flexible barrier. In stage II, a ramp-like dead zone is formed in the flow in Fig. 1b, showing the signature of the runup mechanism; meanwhile, the front of the flowing layer over the dead zone impacts onto the barrier and then either bounces back as a reflected wave or shoots up along the barrier depending on the flow velocity v_0 and the flow-barrier height ratio h_0/H_B . By contrast, a wedge-shaped dead zone is commonly observed in the pile-up mechanism case in Fig. 1d where the flowing layer may hardly directly impact the barrier before settling down to form a new layer of the dead zone due to its low velocity. In stage III, the dead zone in both types of flows is enlarged as more overlying debris mass is deposited with a shape (i.e. ramp-like or wedge-like) largely similar to that in stage II, until overtopping flow over the barrier is observed for both cases at the end of stage III.

Differentiating the different impact mechanisms of geophysical flows serves as a critical theoretical basis for developing analytical models for the design of a flexible barrier. There are indeed certain attempts on

establishing analytical models based on either the runup mechanism (Brighenti et al., 2013; Song et al., 2017) or the pile-up mechanism (Albaba et al., 2018; Faug, 2015) or both (Ashwood and Hungr, 2016; Choi et al., 2015; Zhou et al., 2020). However, it is important to recognize that the runup and pile-up mechanisms for the consideration in a proper analytical model are never as simple as shown in Fig. 1 but depend on a wide range of complex flow conditions (Choi et al., 2015; Song et al., 2018), ranging from flow composition and rheology, channel geometry and surface characteristics, the permeability and deformability of barriers, among others. The current practice of identification of the runup and pile-up mechanisms is predominantly based on macroscopic observations (e.g. Ashwood and Hungr, 2016; Zhou et al., 2020), which may involve subjective judgments and personal experience and thus are sometimes inconsistent (e.g. Ashwood and Hungr, 2016; Song et al., 2018). There remains no clear criterion available that is built upon systematic studies or sound theoretical basis for the identification between the runup and pile-up mechanisms.

There have been large-scale and small-scale experiments and numerical studies investigating the impact behavior of geophysical flows against flexible barriers. Full-scale and large-scale tests (e.g. Brighenti et al., 2013; Bugnion et al., 2012; Ferrero et al., 2015; Wendeler et al., 2006) have been conducted to examine the impact processes which offer valuable data for validating analytical impact models. Small-scale laboratory experiments, serving as a rational, economical alternative, have been developed to investigate key controlling factors of the impact mechanism under well-controlled conditions (e.g. Canelli et al., 2012; Song et al., 2017; Wendeler et al., 2019). For example, Song et al. (2017) conducted a series of flume tests to examine the effect of flow solid fraction on the transition from a pile-up mechanism to a runup mechanism. Notably, however, it has been common that oversimplified flexible barriers were used in these small-scale experiments, including uniform plastic meshes (Wendeler et al., 2019) and impermeable membranes (Ashwood and Hungr, 2016; Song et al., 2019), which indeed expedites the convenience for testing but may not properly reflect the nonuniformity and permeability of a typical flexible barrier

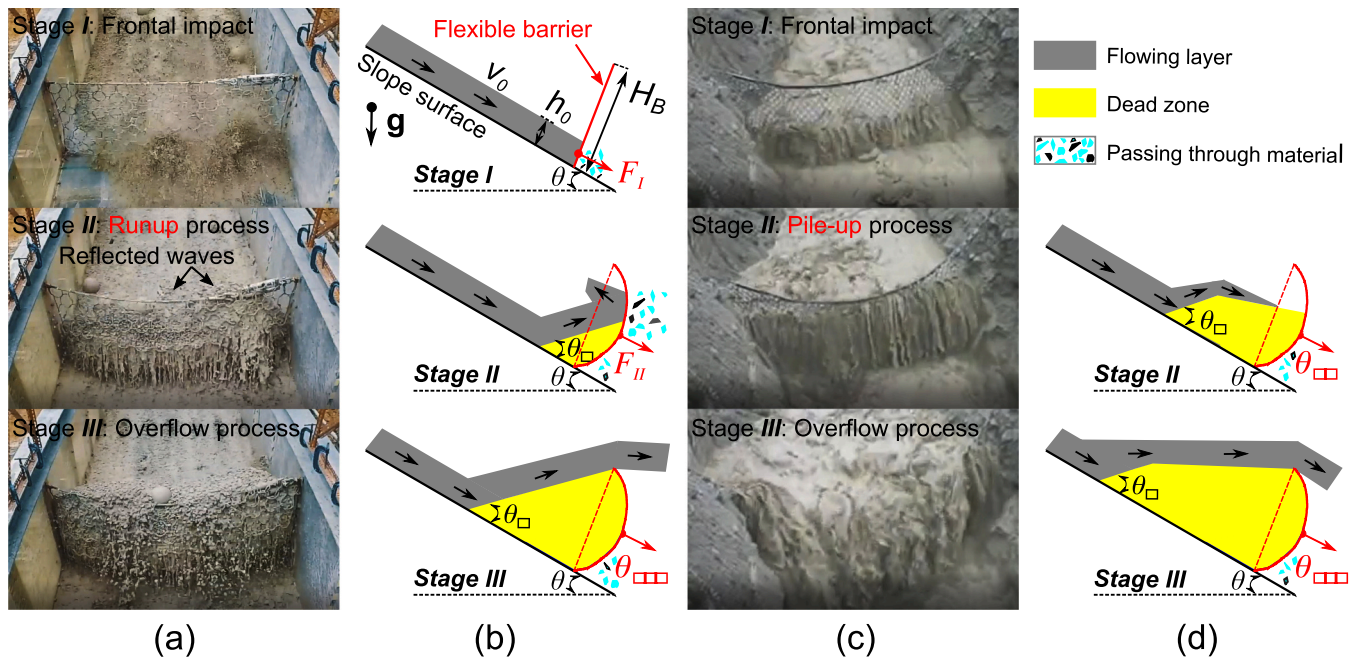


Fig. 1. Illustration of two impact mechanisms, runup (a, b) and pile-up (c, d), of a flexible barrier against multiphase geophysical flows. (a) and (c) show the large-scale flume test in Hong Kong (HKUST, 2019) and the full-scale field test in Switzerland (18 May 2006 debris flow event, Geobruigg, 2012), respectively. (b) and (d) are schematic of the vertical cross-sections presenting runup and pile-up mechanisms, respectively. v_0 and h_0 respectively denote the pre-impact flow velocity and flow thickness. H_B is the original height of the flexible barrier. θ and θ_d denote the channel inclination and the wedge angle of the dead zone, respectively. g denotes the gravitational acceleration.

and thus its intricate interactions with multi-phase debris flows (Pudasaini, 2012; Pudasaini and Mergili, 2019) during the impact process (Kattel et al., 2018; Liu et al., 2020a). Meanwhile, various numerical approaches have been developed to simulate geophysical flows against flexible barriers, including discrete methods (e.g. Discrete element method (DEM), Albaba et al., 2017, 2019), continuous methods (e.g. Finite element method (FEM), Yu et al., 2019; Material Point Method (MPM), Ng et al., 2020), and coupled frameworks (e.g. Lattice Boltzmann Method (LBM) coupled with DEM and FEM, Leonardi et al., 2016; coupled FEM-DEM, Liu et al., 2020b). However, geophysical flows have commonly been simulated as continuum mixture flows or dry flows (Albaba et al., 2017, 2019; Liu et al., 2020b; Ng et al., 2020; Yu et al., 2019). For example, a recent study by Pudasaini and Mergili (2019) presents a multi-phase, multi-mechanical model that is capable of capturing dynamic interactions among various materials and is applicable for different geophysical flows, from avalanches to debris flows to debris floods. Another notable exception is the study by Leonardi et al. (2016) where a coupled LBM-DEM-FEM investigation was performed to capture the solid phase (by DEM) and the fluid phase (by LBM) in a debris flow, and a flexible barrier simulated as a membrane (by FEM). Nevertheless, the membrane therein has been considered non-permeable for the solid phase in debris flow and the interaction between the fluid phase and the barrier has not been taken into account.

In this study, we employ a coupled computational fluid dynamics and discrete element method (CFD-DEM) to uniformly consider the multi-phase, multi-way interactions during the impact of a wide range of geophysical flows (Table 1) on a permeable and nonuniform flexible barrier and to quantitatively examine the runup and pile-up mechanisms and their transitions. The methodology and model setup will be briefly introduced in Sect. 2. In Sect. 3, both flow features (e.g. dead zone formation and flowing layer behavior) and barrier responses (e.g. sustained force and barrier deformation) will be used to characterize the runup and pile-up mechanisms. In Sect. 4, impact mechanism transitions will be quantitatively identified with two newly proposed nondimensional indices, namely, static-peak load ratio and momentum reduction ratio, which are based on the sustained load in barrier cables and momentum change of the flow, respectively. The analysis in this study may help offer clearer identification of the runup and pile-up mechanisms towards the future development of robust analytical models in the design of flexible barriers for mitigating different geophysical flows.

2. Methodology and model setup

A unified approach based on coupled CFD-DEM is employed for the study. For a given geophysical flow composed of solid particles and viscous fluid, the CFD-DEM approach resolves its mixture nature by treating the solid and fluid systems with DEM and CFD, respectively, and solving the intricate inter-phase solid-fluid interactions by exchanging interaction forces and other information (e.g. particle position and momentum) between DEM and CFD (Zhao and Shan, 2013). The DEM can meanwhile be used to treat a nonuniform and permeable flexible barrier consisting of a barrier net, supporting cables, and brakes. Consequently, the multi-way, multi-phase interactions during a typical impact process of such flow onto a flexible barrier, including in-flow solid to solid, in-flow solid-fluid, debris solid and barrier component, debris fluid and barrier component, and between barrier component interactions, can be conveniently captured in a unified manner within the CFD-DEM framework. Note that the unresolved CFD-DEM is employed in this study to offer a balance between computational efficiency and accuracy.

This unresolved CFD-DEM coupling approach has been benchmarked with classic geomechanics problems (Zhao and Shan, 2013; Li and Zhao, 2018a), and is capable of capturing complicated fluid-solid interactions in various engineering conditions including the flow-barrier interactions (Kong et al., 2021; Li and Zhao, 2018b; Li et al., 2020a, 2020b). For instance, this method has been extended to examining impacts of debris

flow on flexible barriers (Li and Zhao, 2018b; Li et al., 2020b), where the modeling of different barrier components has been elaborated, calibrated and verified. Built upon these bases, the focus of this study will be placed on examining the transition of impact mechanisms of a wide spectrum of geophysical flows with a broad range of Froude numbers against a flexible barrier. In what follows, the key ingredients of coupled CFD-DEM modeling of geophysical flows, flexible barriers, and their interactions will be briefly introduced.

2.1. Modeling of the fluid system, solid system and their interactions in geophysical flows

The flow of the fluid system (i.e. air or viscous liquid composed of water and fine-solid materials) in a geophysical flow is simulated by the CFD. The following continuity equation and locally averaged Navier-Stokes equation are solved for the fluid in each cell:

$$\frac{\partial(\epsilon_f \rho_f)}{\partial t} + \nabla \cdot (\epsilon_f \rho_f \mathbf{U}^f) = 0 \quad (1)$$

$$\frac{\partial(\epsilon_f \rho_f \mathbf{U}^f)}{\partial t} + \nabla \cdot (\epsilon_f \rho_f \mathbf{U}^f \mathbf{U}^f) = -\nabla p - \mathbf{f}^p + \epsilon_f \nabla \cdot \boldsymbol{\tau} + \epsilon_f \rho_f \mathbf{g} + \mathbf{f}^s \quad (2)$$

where \mathbf{U}^f and p are the averaged velocity and pressure for the fluid in a cell, respectively. \mathbf{g} is the gravitational acceleration. $\epsilon_f = v_{\text{void}}/v_c$ denotes the void fraction or porosity. v_{void} is the total volume of the void in a cell which may contain either air or liquid or both. v_c is the cell volume. Note that the porosity calculation method refers to Zhao and Shan (2013). \mathbf{f}^p is the fluid-solid interaction force acting on the fluid in a cell imposed by particle(s) inside the cell. The surface tension force \mathbf{f}^s is based on the Continuum Surface Force (CSF) model by Brackbill et al. (1992). The stress tensor $\boldsymbol{\tau}$ in three dimensions for Newtonian and non-Newtonian fluids are reduced to the following functions. The constitutive equation of a Newtonian fluid reads as:

$$\boldsymbol{\tau} = \mu_f \dot{\boldsymbol{\gamma}} \quad (3)$$

where $\boldsymbol{\tau}$, μ_f , $\dot{\boldsymbol{\gamma}}$ are the shear stress, viscosity, shear rate of the fluid, respectively. Compared to water simulated as a Newtonian fluid (Li and Zhao, 2018b; Shan and Zhao, 2014), the viscous-plastic slurry further considered in this study is treated as a more complicated non-Newtonian fluid modeled with the Herschel-Bulkley model (Huang and Garcia, 1998; Pudasaini and Mergili, 2019):

$$\boldsymbol{\tau} = \tau_0 + \kappa \dot{\boldsymbol{\gamma}}^n \quad (4)$$

where τ_0 and κ are the yield stress and consistency index of the fluid, respectively. n is the flow index of the fluid. $n > 1$ gives a shear-thickening fluid while $n < 1$ corresponds to a shear-thinning fluid. $n = 1$ leads to a Bingham fluid. Slurry and mud flow normally have a flow index smaller than 1 (Remaitre et al., 2005).

The solid system of geophysical flows is modeled by the DEM (Cundall and Strack, 1979). The translational and rotational motions of each particle i are governed by the following Newton's equations:

$$m_i \frac{d\mathbf{U}_i^p}{dt} = \sum_{j=1}^{n_i^c} \mathbf{F}_{ij}^c + \mathbf{F}_i^f + \mathbf{F}_i^g \quad (5)$$

$$I_i \frac{d\boldsymbol{\omega}_i}{dt} = \sum_{j=1}^{n_i^c} (\mathbf{M}_{r,ij} + \mathbf{M}_{r,ij}) \quad (6)$$

where m_i and I_i are the mass and moment of inertia of particle i , respectively. \mathbf{U}_i^p and $\boldsymbol{\omega}_i$ denote the translational and angular velocities of particle i , respectively. n_i^c is the total number of contacts for particle i . \mathbf{F}_{ij}^c , $\mathbf{M}_{t,ij}$ and $\mathbf{M}_{r,ij}$ are the contact force (Li and Zhao, 2018b), tangential torque and rolling torque imposed on particle i from particle j or the walls, respectively. \mathbf{F}_i^g is the gravitational force acting on the particle i . \mathbf{F}_i^f is the fluid-particle interaction force acting on the particle i .

The fluid-solid interactions are considered by exchanging interaction

forces \mathbf{F}^f between the CFD and DEM computations. Four interaction forces are considered, including buoyancy force \mathbf{F}^b , drag force \mathbf{F}^d , virtual mass force \mathbf{F}^{vm} and viscous force \mathbf{F}^v (Zhou et al., 2010; Zhao and Shan, 2013):

$$\mathbf{F}^f = \mathbf{F}^b + \mathbf{F}^d + \mathbf{F}^{vm} + \mathbf{F}^v \quad (7)$$

Details of these fluid-solid interaction forces can be found in the literature (Di Felice, 1994; Zhao and Shan, 2013; Zhou et al., 2010) which will not be repeated here for brief. Interested readers can find other advanced analytical models (e.g. Pudasaini, 2019a, 2019b) on the fluid-solid interaction forces, including drag and virtual mass forces.

A sequential iterative procedure is followed for the coupling procedures between the DEM and the CFD computations. At each time step, the DEM first provides such information as the velocities and positions of particles. The positions of all particles are then matched with the fluid cells to calculate relevant information (e.g. porosity and assembled momentum source term $\mathbf{f}^p = \frac{1}{v_c} \sum_{i=1}^{n_c} \mathbf{F}_i^f$) of each cell. When all state variables (e.g. averaged velocity and pressure) for each fluid cell are resolved by the CFD, the particle-fluid interaction forces acting on the centroid of each particle are updated and transferred back to the DEM to solve the particle system for the next time step. Detailed solution procedures can be found in Zhao and Shan (2013).

2.2. Modeling a nonuniform and permeable flexible barrier

A typical non-uniform and permeable flexible barrier (Fig. 2a) is modeled in Fig. 2c as one consisting of a barrier net, supporting cables, and brakes. In particular, the barrier net consists of hexagonal meshes (Fig. 2b), whose opening is designed according to the particle size of the solid phase in a geophysical flow. Ideally, the barrier should be able to block large solid particles while allowing small particles and fluid to pass through. Cables are designed to sustain the load transferred from the barrier net and to transform the load to anchored boundaries. The bottom and lateral edges of the barrier are fixed to mimic the anchored boundaries in the field (Fig. 2c). To reduce the peak impact load, brakes are embedded at the ends of the cables to help dissipate impact energy during the impact.

All the barrier components are modeled with DEM by using particles connected with parallel bonds (Figs. 2b, c and d). As shown in Fig. 2b, a typical hexagonal mesh in a barrier net is simulated by six nodal particles and six parallel bonds, which are placed at the vertexes and the edges of the hexagon, respectively. The bonds link the nodal particles to form a hexagonal mesh. Different bond properties (i.e. stiffness and strength) are adopted for the modeling of the double-twist wires (vertical in Fig. 2b) and the single wires (inclined in Fig. 2b). The total mass of the barrier net is assumed to be distributed onto these particles, according to which their density is adjusted. Similarly, a cable is modeled with a set of connected particles whose centers are along the cable

(Fig. 2c). A brake is modeled with two particles connected by a parallel bond. Importantly, different types of parallel bonds can be adopted to capture various behaviors of the barrier components. Both the barrier net and cables are assumed to be elastic responses with constant stiffness and are simulated with parallel bonds following a linear force-displacement relation (Li and Zhao, 2018b). The brakes are modeled with parallel bonds governed by a tri-linear force-displacement law, which captures the changing stiffness of brakes at different load levels (Li et al., 2020b).

As shown in Fig. 2d, a parallel bond can sustain the axial and shear-directed forces and moments, which are denoted by \bar{F}^n , \bar{F}^s and \bar{M}^n , \bar{M}^s , respectively. Specifically, five parameters are used to define a parallel bond: the normal and shear stiffnesses per unit area, \bar{k}^n and \bar{k}^s ; the tensile and shear strengths, $\bar{\sigma}_c$ and $\bar{\tau}_c$; and the bond-radius multiplier $\bar{\lambda}$. The radius of a parallel bond \bar{R}_{A-B} is defined as $\bar{R}_{A-B} = \bar{\lambda} \min(R_A, R_B)$, where R_A and R_B are radii of two remotely connected particles A and B. Interested readers may refer to some early studies (Li and Zhao, 2018b; Potyondy and Cundall, 2004) for detail of the bond model. The full model description (i.e. flexible barrier system and key components), calibration and validation can be found in Li and Zhao (2018b) and Li et al. (2020b).

Note that the interaction between the barrier particles and the fluid in a debris mixture can be considered in the same manner as the interaction between the solid particles and the fluid in the debris mixture, whereas the interaction between barrier particles and debris particles can be naturally executed under the same umbrella of the DEM. In other words, the solid particles and the fluid in a geophysical flow can exert load on barrier particles via interparticle contact force \mathbf{F}_{ij}^c and fluid-solid interaction force \mathbf{F}^f , respectively. Consequently, this proposed CFD-DEM model offers a direct, unified framework to handle the three-way interactions among the solid, fluid, and flexible barrier.

2.3. Model setup and case plan

Fig. 3 illustrates the model setup for the CFD-DEM simulations of geophysical flows impacting on a flexible barrier, where a flow consisting of solid and fluid phases is taken as an example. A mixture sample ($H_p = 0.55$ m, $L_p = 20$ m, $W_B = 1.2$ m) with a velocity of v_0 is initially placed at the top of the flow channel before being released to flow down the slope under gravity and further impacting against the flexible barrier. The solid and fluid systems of the mixture are assumed as tridisperse grains and a viscous liquid (Fig. 3b), respectively. As shown in Fig. 3a, the CFD domain is bounded by an upper atmosphere face, an outlet face at the end of the channel and four channel walls with an assumed no-slip boundary condition. At the initial state, only fluid cells in the mixture sample are filled with liquid, while the rest of the CFD domain is assumed to be air. In the DEM simulation, the sides and bottom of the flow channel are modeled as fixed, rigid, and frictional walls

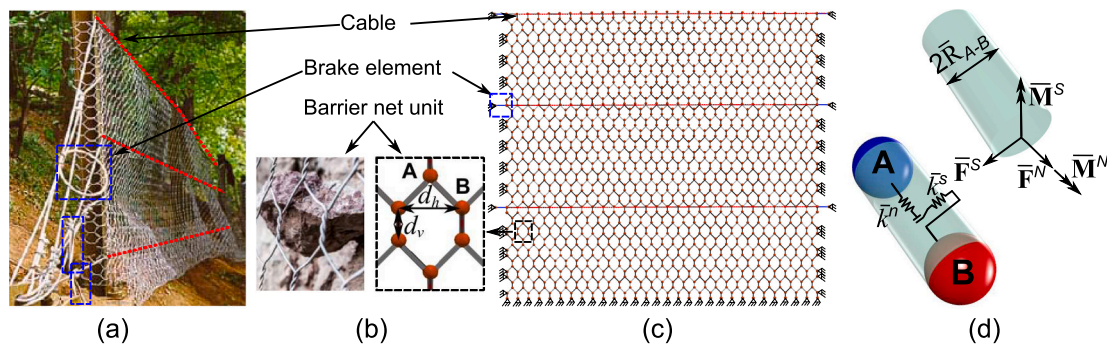


Fig. 2. Model setup for a flexible barrier. (a): A field flexible barrier with hexagonal-shaped net units, cables and brakes in Scottish (Winter et al., 2009); (b): Comparison of the hexagonal-shaped barrier net units in practice and DEM simulation; (c): Configuration of the simulated flexible barrier; (d): A parallel bond between particles A and B in (b) and its key parameters (see Sect. 2.2).

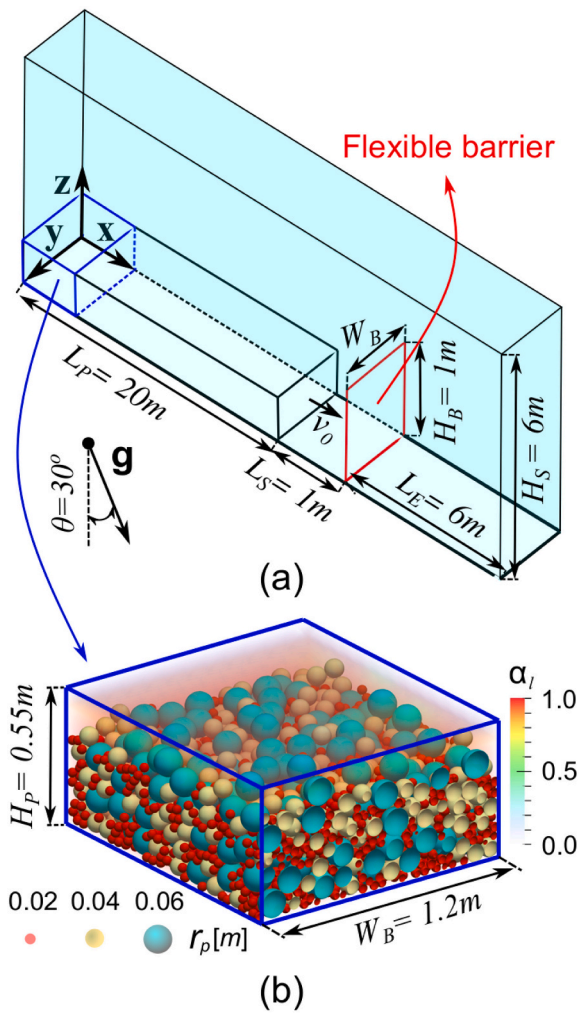


Fig. 3. Model setup for geophysical flows against a flexible barrier. (a): Model geometry prior to the release of the mixture; (b): Illustration of a representative part of the mixture sample consisting of tridisperse particles and a viscous liquid. r_p and α_l denote particle radius and liquid volume fraction, respectively.

with Young's modulus ten times of the particles.

To study the impact mechanisms of different flows, five types of rapid geophysical flows (see Table 1), including rock avalanche, debris avalanche, debris flow, debris flood and mud flow, are considered. There are various criteria for the classification of geophysical flows (Coussot and Meunier, 1996; Hungr et al., 2001). This study focuses on the different material components and fluid models that distinguish various geophysical flows. The five types of geophysical flows are modeled by using different solid volume concentrations and fluid rheological properties as summarized in Table 2. The solid volume concentration ε_s is defined as the ratio between the solid volume and the total volume of a solid-liquid mixture, ranging from 0.1 to 1 in reference to the typical values of geophysical flows (Coussot and Meunier, 1996; Hungr et al., 2001; Iverson, 1997). Rheological properties of the fluid phase in different geophysical flows can be distinguished empirically (Coussot and Meunier, 1996; Pierson, 2005) or mechanically (Pudasaini and Mergili, 2019). As listed in Table 2, the fluid phases in mud flows, debris flows and debris avalanches are modeled as non-Newtonian slurries (Huang and Garcia, 1998; Rémaitre et al., 2005), while water is adopted to model debris floods. Rock avalanches are simulated as dry granular flows. Except for mud flows, a gap-graded tridisperse particle sample is adopted for the solid phase in these geophysical flows. The mass percentages of the particles with radii r_p equal to 0.06 m, 0.04 m, and 0.02 m are 50%, 40%, and 10%, respectively. A monodisperse packing of

Table 2

Test program for the coupled CFD-DEM simulations.

Flow type (Group ID)	Fluid phase	Particle number	ε_s [%]	v_0 [m/s]	Test ID with $v_0 = 6$ m/s
Mud flow (MF)	Slurry 1	39,392	10	1, (1.5), 2, 4, 6, 8, 10, 12, 14, 16	MFV6
Debris flood (DFD)	Water	16,984	20	1, 2, (3), 4, 6, 8, 10, 12, 14, 16	DFDV6
Debris flow (DFWS20)	Slurry 2	16,984	20	1, 2, (3), 4, 6, 8, 10, 12, 14, 16	DFWS20V6
Debris flow (DFWS35)	Slurry 2	29,720	35	1, 2, (3), 4, 6, 8, 10, 12, 14, 16	DFWS35V6
Debris flow (DFWS50)	Slurry 2	42,458	50	1, 2, 4, (5), 6, 8, 10, 12, 14, 16	DFWS50V6
Debris avalanche (DA)	Slurry 2	48,034	68	1, 2, 4, (5), 6, 8, 10, 12, 14, 16	DAV6
Rock avalanche (RA)	None	48,034	100	1, 2, 4, 6, (7), 8, 10, 12, 14, 16	RAV6

particles with $r_p = 0.02$ m is adopted for mud flows to ensure that the particles are smaller than the barrier net opening (i.e. $d_v = 0.02$ m, $d_h = 0.04$, see Fig. 2b) during the impact and thus allow the passage of the particles.

The adopted particle sizes of the geophysical flows are determined according to the scale of the model setup in Fig. 3. The particle number along the flow width direction needs to be sufficiently large to avoid boundary effect from the lateral walls and meanwhile small enough to save computational cost. Moreover, we have explicitly simulated the small particles ($r_p = 0.02$ m) to naturally recover their interactions with the large particles and the liquid in a geophysical flow as well as the barrier. Consideration of small particles into the slurry phase of a geophysical flow could save computational cost but needs careful calibration and validation to recover the flow and impact behavior.

Having generated the five types of geophysical flows, seven test groups are conducted (Table 2), namely, MF, DFD, DFWS20, DFWS35, DFWS50, DA, and RA. For the convenience of discussion, test IDs are assigned to different cases according to their flow type, ε_s and v_0 . As exemplified in Table 2, tests DFWS35V6 and DAV6 denote the numerical tests of debris flow ($\varepsilon_s = 35\%$, $v_0 = 6$ m/s) and debris avalanche ($v_0 = 6$ m/s), respectively. The pre-impact velocities of flows in each group are varied from 1 m/s to 16 m/s to obtain a wide range of Froude numbers (0.46–7.40). The Froude number is defined as $Fr = v_0 / \sqrt{gh \cos \theta}$ (see Caption in Fig. 1b), which is universally adopted in the design of flexible barriers for mitigating geophysical flows such as debris flows (Wendeler et al., 2019; Wendeler and Volkwein, 2015). The obtained range of Fr is generally consistent with that of debris flows in the field, which is from 0.5 to 7.6 (e.g. Hong et al., 2015; Wendeler et al., 2019; Zhou et al., 2020). Note that, in the column of v_0 in Table 2, the flow velocities listed in the brackets correspond to additional cases that are added to accurately identify the mechanism transitions between runup and pile-up, which will be detailed in Sect. 4.2. The adopted model parameters are summarized in Table 3.

This study employs small-scale simulations instead of real-scale ones for computational efficiency. Their dynamic similarity with real-scale geophysical flows is guaranteed by Froude similarity (Li et al., 2020b; Wendeler et al., 2019). Note that for each simulation case, the computation time on an 8-core Intel CPU (3.7 GHz) desktop computer varies from 20 h to 192 h, depending on the particle number in the geophysical flows (16,984–48,034) and the simulated real-time (2–12 s). The size of the simulated flexible barrier was determined according to the scale of the setup in Fig. 3. The barrier mesh size ($d_v = 0.02$ m, $d_h = 0.04$ m, see

Table 3

Key parameters adopted in the coupled CFD-DEM simulations.

Item	Parameter	Value(s)
Particle in a flow	Density * [kg/m ³]	2650
	Radius [m]	0.02, 0.04 and 0.06
	Young's modulus (particle-particle contact) [GPa]	70
	Young's modulus (particle-wall contact) [GPa]	700
	Poisson's ratio *	0.3
	Restitution coefficient *	0.35
	Interparticle friction coefficient	0.7
	Particle-wall friction coefficient	0.5
	Interparticle rolling friction coefficient *	0.15
	Particle-wall rolling friction coefficient *	0.15
Air *	Density [kg/m ³]	1
	Viscosity [Pa·s]	1.48×10 ⁻⁵
Water *	Density [kg/m ³]	1000
	Viscosity [Pa·s]	0.001
Slurry 1 [#]	Density [kg/m ³]	1900
	Consistency index [Pa·s ⁿ]	120
	Flow index	0.34
	Yield stress [Pa]	230
Slurry 2 [#]	Density [kg/m ³]	1365
	Consistency index [Pa·s ⁿ]	21.30
	Flow index	0.24
	Yield stress [Pa]	17.86
Particle in a barrier [†]	Diameter [m]	0.01
	Density [kg/m ³]	5300
	Young's modulus [GPa]	10
	Poisson's ratio	0.3
	Restitution coefficient	0.3
Bond in a barrier [†]	Friction coefficient	0.7
	Stiffness of single wire [×10 ⁸ N/m]	2.2
	Stiffness of double-twisted wire [×10 ⁸ N/m]	4.2
	Stiffness of cable [×10 ⁸ N/m]	8
	Stiffnesses of brake at the three stages [×10 ⁸ N/m]	20, 1.3 and 3.2
	Force limits of brake at the three stages [kN]	50, 80 and 100
Simulation control	Time step (DEM) [s]	1×10 ⁻⁷
	Time step (CFD) [s]	1×10 ⁻⁵
	Simulated real time [s]	2–12

Notes

* Refer to the typical values of physical properties for geophysical flows (Iverson, 1997; Shan and Zhao, 2014);

[#] Refer to typical values of the non-Newtonian fluids (Huang and Garcia, 1998; Remaître et al., 2005);

[†] Refer to key parameters in the modeling of wires and cable (Li and Zhao, 2018b) as well as brake element (Li et al., 2020b; Xu et al., 2018). The bond stiffness here is calculated by multiplying the stiffness per unit area (i.e. \bar{k}^n , \bar{k}^s) by the cross-section area of the bond.

Fig. 2) is designed to block large particles in a flow while allowing small particles to pass through, which recovers the major function of a flexible barrier in reality. The barrier parameters should be well calibrated before being implemented to investigate a real-scale flexible barrier. Please note that the scale of the setup (e.g. barrier size and flow size) may affect the permeability, deformability and mechanical characteristics of the barrier, as well as the flow behavior. Therefore, the following discussion will be predominantly based on dimensionless analyses. In Sect. 3, we will characterize the runup and pile-up mechanisms through two representative cases, *DFWS20V2* and *DFWS20V4*, in terms of the flow features and the barrier responses. All the simulated cases will then be analyzed to identify the impact mechanism transitions between the runup and pile-up in Sect. 4.

3. Runup and pile-up mechanisms

3.1. Features of geophysical flows in the runup and pile-up mechanisms

Fig. 4 shows two cases (*DFWS20V2* in a-c and *DFWS20V4* in d-f) with the same flow constituents and different releasing flow velocities at $t = 2$ s. The different flow features are due to the distinct incoming velocities, which give different flow discharges and impact loads on the barrier. Figs. 4a and d demonstrate the three-way interactions among the solid and fluid phases of debris flows and the deformed barrier. The particle velocity fields are shown in Figs. 4b and e for better visualization of the hydrodynamic dead zones coexisting with the flowing layers. The boundary of the dead zones (denoted by black dash-dotted lines in Figs. 4b and e) is approximately determined based on a velocity threshold (i.e. below 5% of v_0) suggested by Faug et al. (2009). Figs. 4c and f present the force chain network of the particles. Note that the metastable dead zone (Kong et al., 2021) is an identifiable region formed at the upstream of the barrier where the solid particles constitute a quasi-static contact structure, presenting a mechanically stable jammed zone. As shown in Fig. 4, the two flows have distinct features in terms of the dead zone formation, the flowing layer, and the contact force network.

As shown in Fig. 4b, the shape of the dead zone in Case *DFWS20V2* is wedge-like and agrees well with the pile-up mechanism observed by Ng et al. (2016) and that illustrated in Fig. 1d. In comparison, Case *DFWS20V4* presents a ramp-like dead zone coexisting with a flowing layer (Fig. 4e), which is consistent with the runup mechanism observed by Song et al. (2018) and that illustrated in Fig. 1b. Furthermore, the flowing layer over the dead zone in the two cases shows a notable difference as well. The flowing layer is significantly thinned from the upstream to the top of the dead zone in Case *DFWS20V2* (Fig. 4b), whereas in Case *DFWS20V4* it does not show much reduction (Fig. 4e). Accordingly, the velocity of the flowing particles tends to vanish along the flow direction in the pile-up case (Fig. 4b), but those flowing particles in the runup case (Fig. 4e) firstly decelerates from the toe of the dead zone before accelerating from the top of the barrier. It is rare to observe direct impacts of debris particles on the flexible barrier in Case *DFWS20V2* (Figs. 4a and b), due to limited debris mass climbing upon the dead zone. In comparison, the flowing debris particles in Case *DFWS20V4* (Figs. 4d and e) have frequent and direct impacts on the top of the barrier. These features indicate that a wedge-like dead zone formed with the pile-up mechanism may serve better in attenuating and dissipating the impact of the incoming flow than a ramp-like dead zone formed with the runup mechanism.

Figs. 4c and f show the interparticle contact force networks of the solid phase in the debris flow and the dead zone for both cases. Strong contact forces are denoted in red thicker lines and weak contact forces in blue and thin lines. As observed in Figs. 4c and f, the contact force networks in the two cases differ from each other in both the shapes of the contact networks and the locations of strong force chains. Case *DFWS20V2* shows strong contact chains at the lower part of the wedge-like dead zone, whereas the strong contact chains in Case *DFWS20V4* occur at both the lower and higher parts of the ramp-like dead zone and the top of the flexible barrier (Fig. 4f). Notably, in both cases, both the static load induced by the dead zone and the dynamic load resulting from the flowing layer can be transferred through the contact networks (Figs. 4c and f) to the flexible barrier. The relative dominance played by the static or dynamic load for the two mechanisms at different stages will be further discussed in Sect. 3.2.

3.2. Barrier responses under impacts of the runup and pile-up flows

As the flow and the barrier are interactively affecting each other during the impact process, the differences of flow features observed from Cases *DFWS20V2* and *DFWS20V4* indicate distinct barrier responses. This is indeed confirmed by Fig. 5 which shows the distribution of the

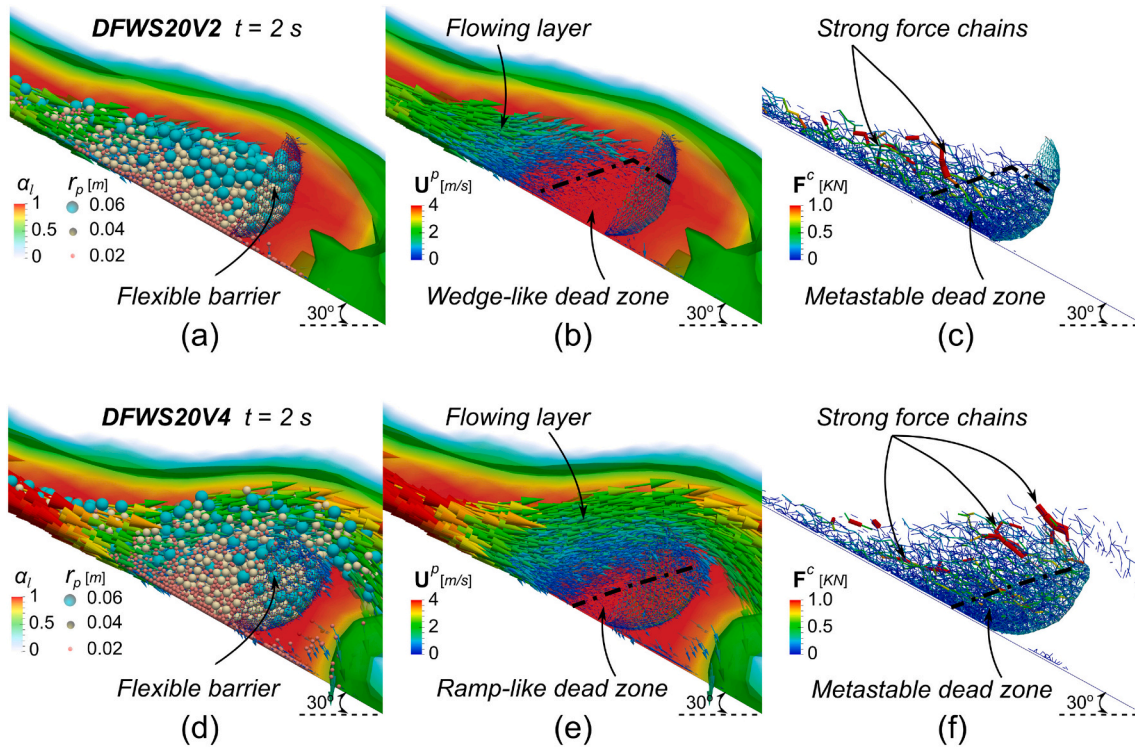


Fig. 4. Comparison of two representative cases of geophysical flows, *DFWS20V2* (a-c) and *DFWS20V4* (d-f), impacting a flexible barrier and the corresponding pile-up and runup mechanisms. The free surface of the liquid in green is determined with liquid volume fraction $\alpha_i = 0.5$. The arrows in the flows indicate the magnitude and direction of particle velocities \mathbf{U}^p . The magnitude of interparticle contact force \mathbf{F}^c is denoted by the thickness and colour. (b) and (e) show the dead zones coexisting with flowing layers. (c) and (f) present the locations of metastable dead zones and strong contact force chains. (For interpretation of the references to colour in this figure legend, the reader is referred to the web version of this article.)

flow-barrier interaction forces (Figs. 5a, b, e and f) and barrier internal bond force (Figs. 5c and g), and the barrier deformation (Figs. 5d and f) at three impact stages (see Fig. 1). Specifically, three forces are considered, including the solid debris-barrier contact force \mathbf{F}_k^{d-f} , the fluid-barrier interaction force \mathbf{F}_k^f , and the barrier internal bond force \mathbf{F}_k^b . The subscript k denotes the initial location of the forces along the barrier height direction. The forces at initial position No. k from 1 to 13 are outputted from the bottom to the upper part of the barrier (Figs. 5a and e). The red solid points denote the initial locations of the cables. \mathbf{F}_k^{d-f} is calculated as $\mathbf{F}_k^{d-f} = \sum_{i \in N} \|\mathbf{F}_{i,k}^{d-f}\|$, where N represents the total number of barrier particles at initial position No. k and $\mathbf{F}_{i,k}^{d-f}$ is the total contact force induced by debris particles acting on barrier particle i at initial position No. k . Analogously, $\mathbf{F}_k^f = \sum_{i \in N} \|\mathbf{F}_{i,k}^f\|$ and $\mathbf{F}_k^b = \sum_{i \in N} \|\mathbf{F}_{i,k}^b\|$. These forces are respectively normalized by their maximum values at the three stages.

The maximum \mathbf{F}_k^{d-f} for Cases *DFWS20V2* and *DFWS20V4* are respectively 1739 N and 2828 N. By contrast, the maximum \mathbf{F}_k^f for Cases *DFWS20V2* and *DFWS20V4* are respectively 116 N and 195 N. Therefore, the impact load acting on a flexible barrier is dominantly induced by the solid debris-barrier contact force \mathbf{F}_k^{d-f} . As shown in Fig. 5a, similar distributions of the \mathbf{F}_k^{d-f} are observed at the three stages in a pile-up case. The \mathbf{F}_k^{d-f} decreases from the bottom to the upper part of the barrier, which is closely related to the static load exerted by the trapped particles in the dead zone (see Fig. 4b and c). Indeed, hydrostatics-based analytical models are recommended for the design of flexible barriers with a pile-up mechanism (e.g. Song et al., 2018). By contrast, the runup case (Fig. 5e) has distinct distribution trends of \mathbf{F}_k^{d-f} at the three stages. The distribution of \mathbf{F}_k^{d-f} in the runup case (Fig. 5e) at stage I is similar to that in the pile-up case (Fig. 5a). However, at stages II and III in the runup case (Fig. 5e), the \mathbf{F}_k^{d-f} sustained at the upper part of the barrier becomes comparable with that at the barrier bottom, differing markedly from the pile-up case. The evolution in Fig. 5e is due to the competitive

roles of the three load components, including the static load induced by the trapped debris (forming a dead zone), the dynamic load from the incoming flow at the toe of the dead zone, and the drag or shear load from the flowing layer above the dead zone. Consequently, hybrid models comprised of both hydrostatic and hydrodynamic components (e.g. Ashwood and Hungr, 2016; Wendeler et al., 2019) are suggested for the design of flexible barriers with a runup mechanism.

Figs. 5b and f further show that the maximum fluid-barrier force \mathbf{F}_k^f appears at stage I for both the pile-up and runup cases. Unlike debris particles that can be effectively blocked by the flexible barrier, the fluid phase of the flows can pass through the barrier. In addition, the \mathbf{F}_k^f tends to decrease from stage I to stage III in Figs. 5b and f, due to the progressive formation of the dead zone at the upstream of the barrier. The dead zone has a low void ratio compared to the flowing material and thus a lower permeability, which decreases the fluid velocity in mitigating the overall impact (Wendeler et al., 2006, 2019).

Figs. 5c and g show the distribution and evolution of the barrier internal bond force \mathbf{F}_k^b in the pile-up and runup cases. In both cases, the \mathbf{F}_k^b increases from stage I to stage III, indicating the dominance of the debris solid-barrier interaction (Figs. 5a and e) over the fluid-barrier interaction (Figs. 5b and f). The maximum impact load acting on the barrier for both the two mechanisms occurs in the overflow stage. Therefore, the loading at stage III should be considered as a critical condition in the design of flexible barriers with overtopping (e.g. the upstream barriers in a multiple-barrier system, Zhang and Huang, 2021). Furthermore, the distributions of \mathbf{F}_k^b in the two cases are similar except for the top parts of the barriers (Figs. 5c and g). In the pile-up case, two local peaks of \mathbf{F}_k^b are observed in the two lower cables at stages II and III (Fig. 5c), indicating effective load transfer from the barrier net to the cables. In comparison, the runup case has three local peaks of \mathbf{F}_k^b at stages II and III (Fig. 5g). The local peak of \mathbf{F}_k^b at the top cable in the runup case (Fig. 5g) is contributed from a large amount of

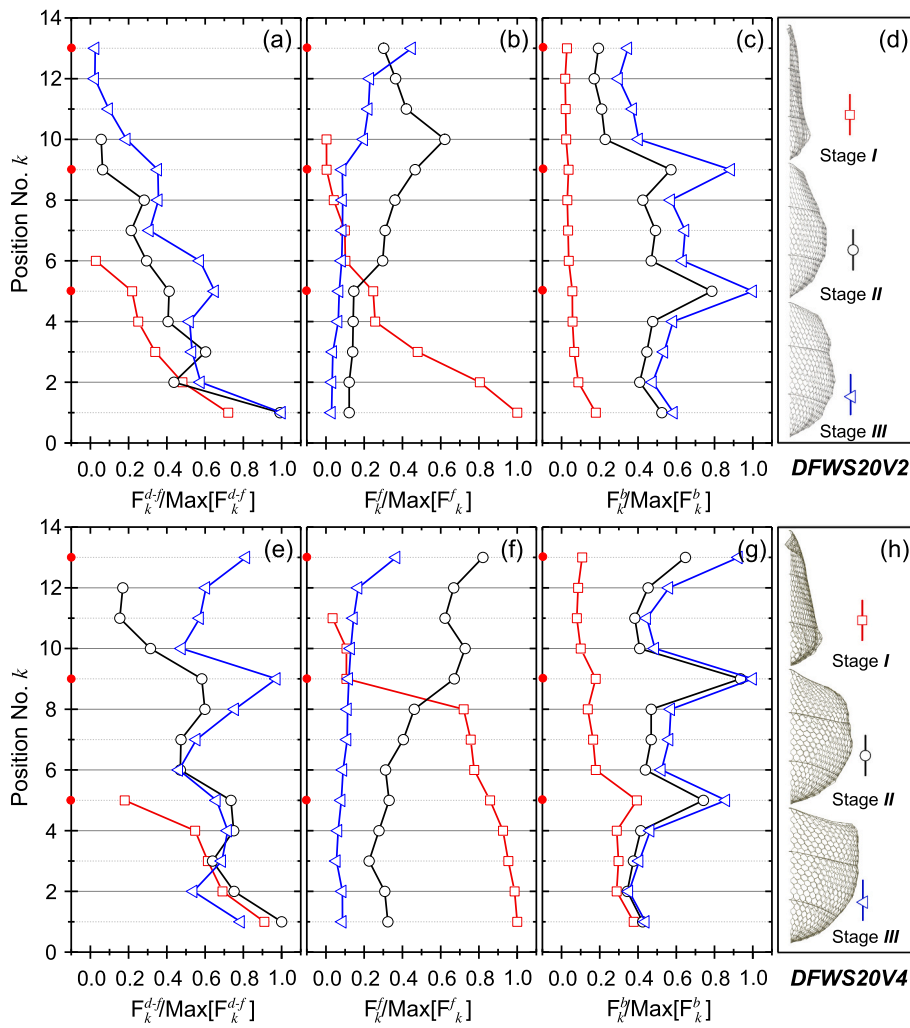


Fig. 5. Comparison of the pile-up (top panel: Case *DFWS20V2*) and runup mechanisms (bottom panel: Case *DFWS20V4*) in terms of flow-barrier interaction forces (a, b, e and f), barrier internal forces (c and g), and the deformed barrier shape (d and h) during stages *I* ($t = 0.4$ s), *II* ($t = 0.8$ s) and *III* ($t = 3$ s). The red solid points on the vertical axis denote the initial positions of cables in a flexible barrier. (For interpretation of the references to colour in this figure legend, the reader is referred to the web version of this article.)

debris mass overtopping the barrier. Importantly, the highest local F_k^b occurs in the cables for both cases, agreeing with experimental and field records (Tan et al., 2018, 2019; Wendeler, 2016).

Figs. 5d and h show that the barrier deformation in Case *DFWS20V4* is larger than that in Case *DFWS20V2* for all three stages. It is due to the larger magnitude of the impact load in the former case, as the flow in Case *DFWS20V4* has larger flow velocity and hence more severe impacts. The maximum elongations of the deformed flexible barriers are observed at stage *III*, as a result of the more deposited debris mass and the more flowing debris impacting on the barrier. Bulges between the cables of the deformed barrier are observed for both cases at stage *II* and *III*, which is consistent with field observations with similar barrier configurations (Geobruigg, 2012; Wendeler, 2016).

4. Transition of impact mechanism between runup and pile-up

Based on the analyses of flow features and barrier responses in Sect. 3, the impact mechanism of a geophysical flow, either runup or pile-up, can be tentatively identified. Nevertheless, as mentioned in the introduction, the identification is sometimes difficult due to various uncertainties involved, especially for cases where transitional impact behavior emerges. In this section, two nondimensional criteria are proposed, based on which the impact mechanisms of all the simulated geophysical flows will be quantitatively examined. It may constitute a first attempt that quantifies the impact mechanism transitions from the perspectives of both the flow behavior and the barrier responses when a

wide spectrum of geophysical flows are considered impacting a flexible barrier. Prior to the discussion of the two criteria, typical flow-barrier interaction processes captured from the simulated seven groups of geophysical flows (see Table 2) are firstly summarized.

4.1. Flow-barrier interaction processes

Fig. 6 shows the three typical impact stages of seven representative geophysical flows impacting against a permeable and deformable flexible barrier. The pre-impact velocity ($v_0 = 6$ m/s) and the Froude number ($Fr = 2.78$) of these flows are identical. The debris-barrier and slurry-barrier interactions in all the cases are reasonably captured as observed in Fig. 6, where the particles and the slurry are intercepted and deflected by the barrier during the impact process. In addition, small solid particles (and fluid if any) pass through the barrier by virtue of the barrier permeability. The impact behavior varies significantly in the seven cases of rapid geophysical flows with different solid volume concentrations ($\epsilon_s = 0.1-1$) and fluid rheological properties. As shown in Figs. 6a and g, the impact behavior in Case *RAV6* ($\epsilon_s = 1$) shows notable differences compared to Case *MFV6* ($\epsilon_s = 0.1$), in terms of the flow-barrier interactions, the formation of the dead zone as well as the overspreading. Furthermore, compared to Case *DFV6* where the fluid phase is water (Figs. 6b), less fluid in Case *DFWS20V6* (Figs. 6c) is found to pass through the barrier, due to the larger viscosity, yield stress and density of the slurry used in the latter case. Indeed, more viscous slurry gives rise to higher shear resistance during its flowing process compared

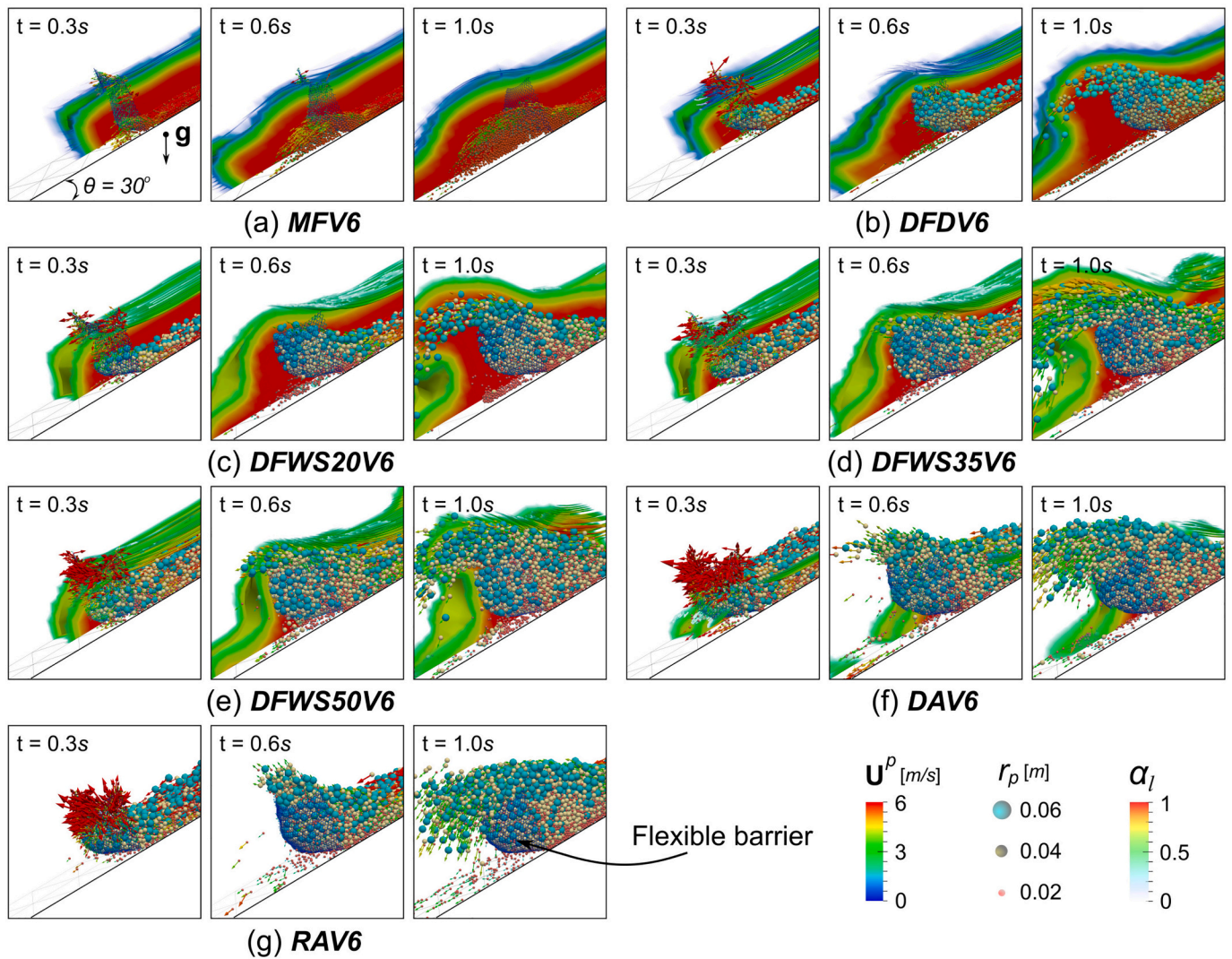


Fig. 6. Snapshots showing the flow-barrier interaction processes for seven typical geophysical flows ($v_0 = 6$ m/s, $Fr = 2.78$) against a flexible barrier. Three typical impact process including stage I (frontal impact, $t = 0.3$ s), stage II (runup or pile-up process, $t = 0.6$ s) and stage III (runup & overflow or pile-up & overflow, $t = 1$ s) are observed. A clip of the fluid system in the middle of the flow channel is presented to better visualize the solid system. See Fig. 4 for detailed captions.

to the water in Case *DFV6* and hence less passing of fluid through the barrier. As shown in Figs. 6c, d and e, an increase of ϵ_s results in more trapped particles in a larger dead zone which more effectively restrains the fluid motion and leads to less fluid overtopping and passing through the barrier.

It should be noted that, in addition to the distinct flow parameters focused in this study, barrier configurations (e.g. number of supporting cables, mesh type, activation force of brakes) may also affect the flow-barrier interaction. Unlike rigid barriers with no notable deflection during the impact, a flexible barrier can rearrange itself during the entire impacting process (Canelli et al., 2012). When subjected to the impact of a geophysical flow, the flexible barrier may deform and reduce in height, which in turn influences the barrier containment capacity and further affects the force sustained in the barrier. This complicated interactive responses between the barrier and the flow complexify the flow-barrier interaction. It is thus important to evaluate the impact mechanism in terms of both the barrier response (i.e. static-peak load ratio in Sect. 4.2) and the flow feature (i.e. momentum reduction ratio in Sect. 4.3).

4.2. Static-peak load ratio of the barrier

According to the distinct signatures of the runup and pile-up impact mechanisms (see Figs. 1, 4 and 5), all the simulated flows are tentatively classified based on their flow features (e.g. dead zone formation and shape, overflowing behavior) and barrier responses (e.g. distribution and evolution of sustained forces). As shown in Fig. 7, the solid and empty symbols denote cases in the pile-up and runup mechanisms determined by numerical observations, respectively. The half-filled symbols (between the black dashed lines in Fig. 7) represent cases in which the impact mechanism is difficult to be determined with subjective judgment and experience.

To identify the impact mechanisms of these unclear cases (half-filled symbols in Fig. 7), the barrier response in terms of the normalized cable force F^{cab}/F_{peak}^{cab} is further examined. Since the cables play a crucial role in supporting the barrier and transferring impact loads to the ropes and anchors, and their tensile forces are normally measured in the field and experiments (Brighenti et al., 2013; Tan et al., 2018, 2020). It is found that these cases with unclear mechanisms have a similar ratio between the static force and the peak force sustained in the cables of the barrier, i. e., $F_{static}^{cab}/F_{peak}^{cab} \cong 0.8$. Therefore, the static-peak load ratio, defined as $\delta = F_{static}^{cab}/F_{peak}^{cab}$, is proposed for the identification of the mechanism

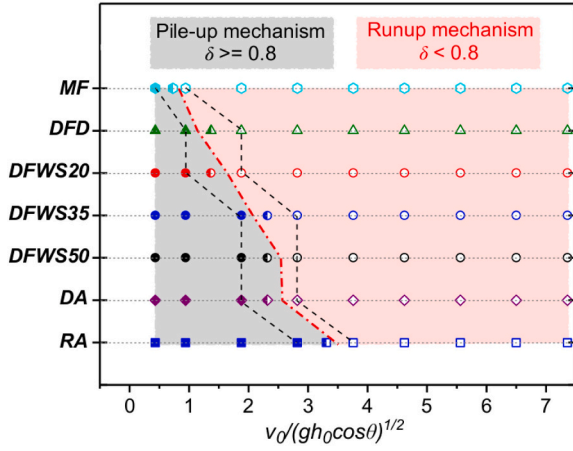


Fig. 7. Mechanism transitions between runup and pile-up determined by numerical observations and the static-peak load ratio $\delta = F_{static}^{cab}/F_{peak}^{cab}$ with a threshold value of $\delta \cong 0.8$. The solid and empty symbols respectively denote cases of the pile-up and runup mechanisms determined by the numerical observations, whilst the half-filled symbols (between the black dashed lines) represent cases showing the transitional impact behavior. Based on the criterion of δ , the gray and pink areas (separated by a red dash-dotted line) further visualize the pile-up and runup mechanisms, respectively. (For interpretation of the references to colour in this figure legend, the reader is referred to the web version of this article.)

transitions with threshold value $\delta \cong 0.8$. Given F^{cab} as the total force sustained in all the three cables of a barrier, F_{static}^{cab} and F_{peak}^{cab} are the static and peak values of F^{cab} , respectively. Specifically, F^{cab} is calculated by $F^{cab} = \sum_{i \in N_t} \|\bar{F}_i\|$, where N_t denotes the total number of nodal particles

in all the three cables at time t . \bar{F}_i is the bond force acting on nodal particle i . When having the temporal evolution of F^{cab} from the entire flow-barrier interaction process, F_{peak}^{cab} is the peak value of the evolution, and F_{static}^{cab} is the value at the end of the evolution. The static load F_{static}^{cab} is mainly contributed from the static debris trapped by the barrier at the end of the impact. The red dash-dot line in Fig. 7 separates the two groups of cases with different δ . The cases with $\delta \geq 0.8$ are characterized as the pile-up mechanism (the gray region in Fig. 7), whereas the cases with $\delta < 0.8$ are recognized as the runup mechanism (the pink region in Fig. 7).

Based on the criterion of δ demonstrated in Fig. 7, the red dash-dotted line shows the critical Fr values at which the impact mechanism transitions happen in seven groups of geophysical flows. The range of the critical Fr is approximately from 0.7 to 3.7, depending on the flow type (i.e. MF, DFD, DFW, DA and RA) and the solid volume concentration ε_s . Furthermore, the effect of ε_s on the impact mechanism transitions can be observed from the three groups of debris flows (i.e. DFWS20, DFWS35 and DFWS50). A larger ε_s of a debris flow tends to give a larger critical Fr at which the transition occurs. Given the same Fr , the increase of ε_s may lead to the transition from the runup to pile-up, as observed from Case DFWS20V4 and Case DFWS35V4 when $Fr = 1.85$ (Fig. 7). Indeed, the larger ε_s in Case DFWS35V4 results in more particles trapped in the dead zones, leading to a larger static force acting on the barrier and thus a higher δ .

It is worthy to note that the criterion with a sharp threshold ($\delta \cong 0.8$) is proposed to offer convenience in identifying different mechanisms to avoid excessive ambiguity. The impact mechanism transitions under the effect of Fr and ε_s are indeed gradual. Taking four simulation cases with different velocities (and thus Fr) as an example, Fig. 8 shows the temporal evolution of the load ratio F^{cab}/F_{peak}^{cab} , where the end of each curve is the static-peak load ratio $\delta = F_{static}^{cab}/F_{peak}^{cab}$. F_{static}^{cab} is measured at the end of the flow-barrier interactions after the impact ends. Cases DFWS20V2 ($\delta = 0.98$, black solid line) and DFWS20V3 ($\delta = 0.82$, green dashed line)

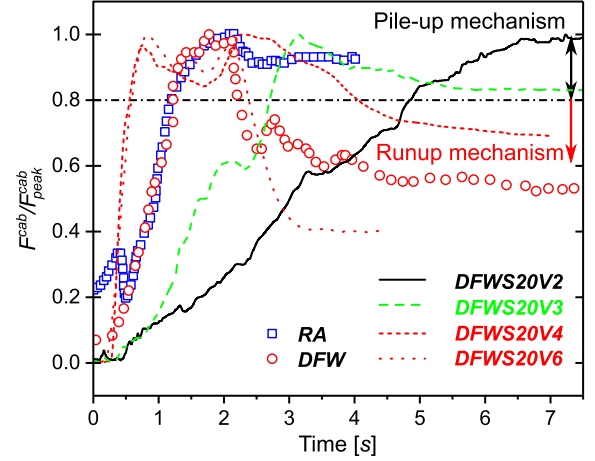


Fig. 8. Load ratio versus time for the large-scale laboratory test RA by Tan et al. (2018), the full-scale field test DFW by Bugnion and Wendeler (2010), and numerical cases DFWS20 with v_0 ranging from 2 m/s to 6 m/s.

undergo the pile-up mechanism, whilst cases DFWS20V4 ($\delta = 0.71$, red short-dashed line) and DFWS20V6 ($\delta = 0.38$, red dot line) experience the runup mechanism. With the increase of v_0 from 2 m/s to 6 m/s, δ gradually decreases from 0.98 to 0.38, showing the gradual transition from the pile-up to runup mechanisms. Note that a higher velocity results in a higher impact force and a larger barrier deformation at rest, and consequently resulting in a reduced barrier height and retainment capacity. In addition to our simulation cases, two flows in different mechanisms from large-scale experiments performed by Tan et al. (2018) and Bugnion and Wendeler (2010) are also illustrated in Fig. 8. The rock avalanche against a flexible barrier in the large-scale laboratory tests (Tan et al., 2018) gives $\delta = 0.92$, indicating the pile-up mechanism. Indeed, the motion of the avalanche and the formation of the ramp-like dead zone reported in Tan et al. (2018) agree reasonably well with the signatures of the pile-up mechanism. The debris flow impacting on a flexible barrier in the full-scale test (Bugnion and Wendeler, 2010) presents $\delta = 0.54$, which is classified as the runup mechanism. The reflected waves observed after the impact on the barrier in Bugnion and Wendeler (2010) are consistent with the runup mechanism. The two experimental cases partly verify the identification of the impact mechanism transition based on $\delta = 0.8$. In addition to the characteristics of anticipated flows, the criterion of static-peak load ratio could differ with varying barrier deformability and configuration, which need to be further explored in the future.

4.3. Momentum reduction ratio of the flow

The momentum reduction of the flow is commonly calculated by assuming no change in the discharge rate along the flow path during the impact process (runup or pile-up with overtopping) (e.g. Ashwood and Hungr, 2016; Song et al., 2019; Zhou et al., 2020). This could be valid to a certain extent for geophysical flows in the runup mechanism when impacting on a rigid barrier. In the flexible barrier case, however, a non-negligible amount of debris would be gradually trapped in the dead zone or continuously pass through the permeable flexible barrier (see Figs. 1a and c). In this study, a momentum reduction ratio $\zeta = (m_{of}v_0 - m_{of}\bar{v}_{of}) / m_{of}v_0 = (v_0 - \bar{v}_{of}) / v_0$ is proposed to quantify the mechanism transition between the runup and pile-up with consideration of the flowing debris that overtops the flexible barrier, by which the momentum change before and after the impact can be calculated for the same flowing debris. Specifically, m_{of} and \bar{v}_{of} respectively denote the mass and mean velocity of a certain amount of flowing debris that firstly overtops the flexible barrier. They are extracted from the overflow

mixtures in the region ($x_B < x < x_B + H_B/2$) at the time instant after 1×10^{-5} s (i.e. 100 DEM steps) of the first overtopping particle and fluid. Note that $H_B/2$ is around the maximum barrier deflection along the x -direction (see the coordinate in Fig. 3a). Therefore, ζ denotes the dissipation ratio of momentum for a certain amount of flowing debris with mass m_{of} , whose momentum is dissipated from its incoming flow path to the top of a barrier. This momentum reduction is mainly contributed by the change of flow potential energy, the friction and collision between the flowing layer and dead zone, and the friction and collision inside the flowing layer. Note that the change in mass during the flow-structure interactions is possibly due to the separation between particles and fluid (Kattel et al., 2018; Pudasaini and Fischer, 2020), which is beyond the scope of this study.

Similar to the determination of $\delta = 0.8$ in Sect. 4.2, the critical momentum reduction ratio for the impact mechanism transition is determined as $\zeta = 0.5$, according to the cases showing unclear mechanisms (i.e. half-filled symbols in Fig. 7). The momentum reduction ratios of all the simulated geophysical flows are summarized in Fig. 9. The cases with $\zeta > 0.5$ are characterized as the pile-up mechanism (gray region), while the cases with $\zeta < 0.5$ are identified as the runup mechanism (pink region). The solid and empty symbols in Fig. 9 denote cases respectively identified as the pile-up and runup mechanisms based on the criterion of δ (see Fig. 7). Notably, there are some cases where impact mechanisms are identified differently based on the two criteria (i.e. $\delta = 0.8$ and $\zeta = 0.5$). For instance, Case DFWS20V3 (red solid circle below the dash-dot line in Fig. 9) is characterized as the pile-up mechanism based on its $\delta = 0.82$ but is recognized as the runup mechanism using its $\zeta = 4.85$. Besides, there are two empty symbols above the dash-dot line in Fig. 9, indicating the conflicting mechanisms identified based on the two criteria. These cases where the two criteria give different mechanisms are indeed close to the transition line (a red dash-dotted line in Fig. 9) since the proposed two criteria are made artificially sharp. Therefore, if the impact mechanism of a flow is determined differently with the two criteria, it may well indicate that the flow is close to the mechanism transition, under which condition both mechanisms should be carefully analyzed to choose the conservative one for practical design.

Moreover, Fig. 9 reveals the effects of Froude number Fr and solid volume concentration ϵ_s on ζ for seven groups of geophysical flows. For

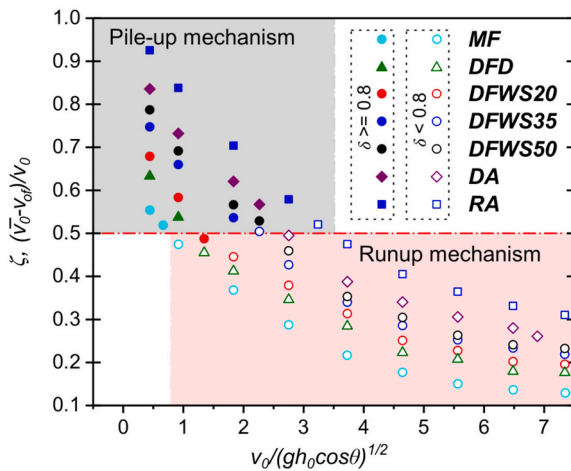


Fig. 9. Mechanism transitions between runup and pile-up quantified by the momentum reduction ratio $\zeta = \frac{(v_0 - \bar{v}_{of})}{v_0}$ with a threshold value of $\zeta \cong 0.5$. The gray and pink regions (separated by a red dash-dotted line) visualize the pile-up and runup regimes based on the $\zeta - Fr$ correlations, respectively. Solid and empty symbols of the tests respectively denote the identified pile-up and runup mechanisms according to the criterion of δ (see Fig. 7). (For interpretation of the references to colour in this figure legend, the reader is referred to the web version of this article.)

each type of geophysical flows, ζ decreases with Fr , while the decreasing rate reduces and tends to vanish with the growth of Fr . A higher Fr indicates a larger flow velocity, which leads to a flowing layer that over-rides the dead zone and overtops the barrier with less momentum reduction. This may imply that the mitigation efficiency of a resisting flexible barrier tends to reduce with the increase of Fr of the geophysical flows. Furthermore, the vertically aligned data points (from group MF to group RA) in Fig. 9 demonstrate a significant effect of ϵ_s . The higher the solid volume concentration ϵ_s , the larger the momentum reduction ratio ζ . This might be related to the different efficiency of solid particles and fluids in dissipating energy. Indeed, grain shear stress (friction and collision) is commonly considered as more effective in energy dissipation compared to fluid viscous shearing during the debris-structure interactions (Choi et al., 2015; Song et al., 2017).

5. Discussion and conclusions

This study provides a comprehensive analysis of the impact mechanism transitions for seven groups of geophysical flows against a flexible barrier. To cover a wide range of geophysical flows, the simulated flows are varied in terms of their flow dynamics, components and rheological properties, by which the effects of solid volume concentrations ($\epsilon_s = 0.1-1$), Froude numbers ($Fr = 0.43-7.40$), and fluid rheologies (Newtonian and non-Newtonian), have been investigated. Meanwhile, a flexible barrier is considered as a system consisting of hexagonal-shaped meshes, cables and brake elements. To capture the fundamental three-way interactions among the flexible barrier, the solid and the fluid of flows, a unified CFD-DEM framework has been adopted, in which the fluid is modeled with CFD and the solid in a flow and the barrier are simulated with DEM. Major conclusions are summarized as follows.

1. Two representative debris flows showing the runup and pile-up mechanisms have been thoroughly analyzed to distinguish the signatures of the two mechanisms, from the perspectives of both flow features and barrier responses. In particular, flows in the two mechanisms exhibit distinct characteristics in terms of the shape of the dead zone (i.e. ramp-like shape for runup and wedge-like shape for pile-up), the thickness of the flowing layer, and the locations of strong force chains. Furthermore, the distribution and evolution of the flow-barrier interaction forces and internal forces sustained by the barrier also show a notable difference between the two mechanisms. Based on the study, for the practical design of flexible barriers, hydrostatic-based models are recommended for a pile-up mechanism, and hybrid models are suggested for a runup mechanism. It is also found that the most critical force in the barrier occurs at the overflow stage for both mechanisms, indicating the significance of considering overtopping, especially in the design of multi-level flexible barriers.
2. The typical flow-barrier interaction process has been examined for seven geophysical flows with different constituents. Although the natures of the seven geophysical flows differ, their flow features (e.g. flow deceleration and redirection) and barrier responses (e.g. barrier deformability and permeability) have all been captured by the employed method. Compared to the mixture of water and solid particles (i.e. debris flood), the mixture consisting of slurry and solid particles (i.e. debris flow) has less fluid passing through the barrier. A higher solid volume concentration leads to more particles trapped in the dead zone and more effectively restrains the fluid motion, leading to less overtopping fluid.
3. For the first time, two dimensionless indices, the static-peak load ratio of a barrier (δ) and the momentum reduction ratio of a flow (ζ), have been proposed to identify mechanism transitions between the runup and pile-up for a wide spectrum of geophysical flows with different flow components and Froude numbers. Built upon the two criteria, the critical Froude numbers (Fr) have been quantitatively examined for the impact mechanism transitions in seven groups of

geophysical flows. It is found that the transition from pile-up to runup occurs with an increasing Fr for geophysical flows with the same components. For flows with different components, both the growth of solid volume concentration and the replacement of water by slurry in a solid-fluid mixture lead to a transition occurring at a higher Fr .

This study helps us gain a deeper understanding of the runup and pile-up mechanisms and offers quantitative identification of the mechanism transitions for a wide spectrum of geophysical flows. The analysis in this study may help reduce subjective uncertainties in identifying the two mechanisms and provide analytical bases in flexible barrier design according to anticipated flow dynamics and properties. Note that in reality the impact behavior of a geophysical flow could start with a runup mechanism and transform into a pile-up mechanism (Zhou et al., 2020). Such transitional behavior within a single flow impact will be studied in the future. Furthermore, the mechanism transitions may also be affected by a variety of other factors, including flow composition, successive surges and flow-barrier height ratio, slope inclination, and the configurations and deformability of the flexible barriers. For instance, boulders with destructive power and successive surges could significantly affect the impact behavior (e.g. Albaba et al., 2017; Su et al., 2020). These factors will be a focus of future study.

In this study, the same range of Fr has been adopted for all the investigated types of geophysical flows for consistent model setup and convenient comparison. Nevertheless, extreme Fr might not be realistic for some of the geophysical flows and careful attention should be paid when interpreting the results. For instance, the common Froude-numbers and pre-impact velocities for avalanches and mud flows could be lower than the adopted maximum values (e.g. $Fr = 7.40$, $v_0 = 16$ m/s). Moreover, a direct simulation of a real-scale flow with the proposed coupled CFD-DEM approach may demand too expensive computational cost to be realistic. Alternatively, it may be more efficient and feasible to model real-scale geophysical flows (e.g. Mergili et al., 2020a, 2020b) with advanced continuum mechanics based multi-phase mass flow models (e.g. Pudasaini, 2012; Pudasaini and Mergili, 2019).

Declaration of Competing Interest

The authors declare no competing financial interests or personal relationships that could have appeared to influence the work reported in this paper.

Acknowledgments

The research reported in this study was financially supported by the National Natural Science Foundation of China (Project #11972030) and the University Grants Council of Hong Kong (RGC/GRF Project #16205418, TBRs Project #T22-603/15 N and CRF Project #C6012-15G).

References

- Albaba, A., Lambert, S., Kneib, F., Chareyre, B., Nicot, F., 2017. DEM modeling of a flexible barrier impacted by a dry granular flow. *Rock Mech. Rock. Eng.* 50 (11), 3029–3048. <https://doi.org/10.1007/s00603-017-1286-z>.
- Albaba, A., Lambert, S., Faug, T., 2018. Dry granular avalanche impact force on a rigid wall: analytic shock solution versus discrete element simulations. *Phys. Rev. E* 97 (5), 052903. <https://doi.org/10.1103/PhysRevE.97.052903>.
- Albaba, A., Schwarz, M., Wendeler, C., Loup, B., Dorren, L., 2019. Numerical modeling using an elastoplastic-adhesive discrete element code for simulating hillslope debris flows and calibration against field experiments. *Nat. Hazards Earth Syst. Sci.* 19 (11), 2339–2358. <https://doi.org/10.5194/nhess-19-2339-2019>.
- Ashwood, W., Hungr, O., 2016. Estimating total resisting force in flexible barrier impacted by a granular avalanche using physical and numerical modeling. *Can. Geotech. J.* 53 (10), 1700–1717. <https://doi.org/10.1139/cgj-2015-0481>.
- Brackbill, J.U., Kothe, D.B., Zemach, C., 1992. A continuum method for modeling surface tension. *J. Comput. Phys.* 100 (2), 335–354. [https://doi.org/10.1016/0021-9991\(92\)90240-Y](https://doi.org/10.1016/0021-9991(92)90240-Y).
- Brighenti, R., Segalini, A., Ferrero, A.M., 2013. Debris flow hazard mitigation: a simplified analytical model for the design of flexible barriers. *Comput. Geotech.* 54, 1–15. <https://doi.org/10.1016/j.compgeo.2013.05.010>.
- Bugnion, L., Wendeler, C., 2010. Shallow landslide full-scale experiments in combination with testing of a flexible barrier. *WIT Trans. Sci. Eng.* 67, 161–173. <https://doi.org/10.2495/DEB100141>.
- Bugnion, L., McArdell, B.W., Bartelt, P., Wendeler, C., 2012. Measurements of hillslope debris flow impact pressure on obstacles. *Landslides* 9 (2), 179–187. <https://doi.org/10.1007/s10346-011-0294-4>.
- Canelli, L., Ferrero, A.M., Migliazza, M., Segalini, A., 2012. Debris flow risk mitigation by the means of rigid and flexible barriers - experimental tests and impact analysis. *Nat. Hazards Earth Syst. Sci.* 12 (5), 1693–1699. <https://doi.org/10.5194/nhess-12-1693-2012>.
- Choi, C.E., Au-Yeung, S.C.H., Ng, C.W.W., Song, D., 2015. Flume investigation of landslide granular debris and water runup mechanisms. *Geotech. Lett.* 5 (1), 28–32. <https://doi.org/10.1680/geolett.14.00080>.
- Coussot, P., Meunier, M., 1996. Recognition, classification and mechanical description of debris flows. *Earth Sci. Rev.* 40 (3–4), 209–227. [https://doi.org/10.1016/0012-8252\(95\)00065-8](https://doi.org/10.1016/0012-8252(95)00065-8).
- Cundall, P.A., Strack, O.D., 1979. A discrete numerical model for granular assemblies. *Geotechnique* 29 (1), 47–65. <https://doi.org/10.1680/geot.1979.29.1.47>.
- Di Felice, R., 1994. The voidage function for fluid-particle interaction systems. *Int. J. Multiphase Flow* 20 (1), 153–159. [https://doi.org/10.1016/0301-9322\(94\)90011-6](https://doi.org/10.1016/0301-9322(94)90011-6).
- Faug, T., 2015. Depth-averaged analytic solutions for free-surface granular flows impacting rigid walls down inclines. *Phys. Rev. E* 92 (6), 062310. <https://doi.org/10.1103/PhysRevE.92.062310>.
- Faug, T., Beguin, R., Chanut, B., 2009. Mean steady granular force on a wall overflowed by free-surface gravity-driven dense flows. *Phys. Rev. E* 80 (2), 021305. <https://doi.org/10.1103/PhysRevE.80.021305>.
- Ferrero, A.M., Segalini, A., Umili, G., 2015. Experimental tests for the application of an analytical model for flexible debris flow barrier design. *Eng. Geol.* 185, 33–42. <https://doi.org/10.1016/j.enggeo.2014.12.002>.
- Geobruug, A.G., 2012. Geobruug: Protection systems for rockfall, debris flow, slope instability, mining, avalanche. Accessed October 10, 2020. <https://www.youtube.com/watch?v=LUUeBRZ-10g>.
- Guerreiro, S.B., Fowler, H.J., Barbero, R., Westra, S., Lenderink, G., Blenkinsop, S., Li, X. F., 2018. Detection of continental-scale intensification of hourly rainfall extremes. *Nat. Clim. Chang.* 8 (9), 803–807. <https://doi.org/10.1038/s41558-018-0245-3>.
- HKUST, 2019. HKUST. Accessed October 10, 2020. <https://www.youtube.com/watch?v=wjTjQGMfgpU&list>.
- Hong, Y., Wang, J.P., Li, D.Q., Cao, Z.J., Ng, C.W.W., Cui, P., 2015. Statistical and probabilistic analyses of impact pressure and discharge of debris flow from 139 events during 1961 and 2000 at Jiangjia Ravine. *China. Eng. Geol.* 187, 122–134. <https://doi.org/10.1016/j.enggeo.2014.12.011>.
- Hu, H., Zhou, G.G., Song, D., Cui, K.F.E., Huang, Y., Choi, C.E., Chen, H., 2020. Effect of slit size on the impact load against debris-flow mitigation dams. *Eng. Geol.* 274, 105764. <https://doi.org/10.1016/j.enggeo.2020.105764>.
- Huang, X., Garcia, M.H., 1998. A Herschel-Bulkley model for mud flow down a slope. *J. Fluid Mech.* 374, 305–333. <https://doi.org/10.1017/S0022112098002845>.
- Hungr, O., Evans, S.G., Hutchinson, I.N., 2001. A review of the classification of landslides of the flow type. *Environ. Eng. Geosci.* 7 (3), 221–238. <https://doi.org/10.2113/gsegeosci.7.3.221>.
- Iverson, R.M., 1997. The physics of debris flows. *Rev. Geophys.* 35 (3), 245–296. <https://doi.org/10.1029/97RG00426>.
- Kattel, P., Kafle, J., Fischer, J.T., Mergili, M., Tuladhar, B.M., Pudasaini, S.P., 2018. Interaction of two-phase debris flow with obstacles. *Eng. Geol.* 242, 197–217. <https://doi.org/10.1016/j.enggeo.2018.05.023>.
- Kong, Y., Zhao, J.D., Li, X.Y., 2021. Hydrodynamic dead zone in multiphase geophysical flows impacting a rigid obstacle. *Powder Technol.* 386, 335–349. <https://doi.org/10.1016/j.powtec.2021.03.053>.
- Leonardi, A., Wittel, F.K., Mendoza, M., Vetter, R., Herrmann, H.J., 2016. Particle-fluid-structure interaction for debris flow impact on flexible barriers. *Comput. Aided Civ. Infrastruct. Eng.* 31 (5), 323–333. <https://doi.org/10.1111/mice.12165>.
- Li, X., Zhao, J., 2018a. Dam-break of mixtures consisting of non-Newtonian liquids and granular particles. *Powder Technol.* 338, 493–505. <https://doi.org/10.1016/j.powtec.2018.07.021>.
- Li, X., Zhao, J., 2018b. A unified CFD-DEM approach for modeling of debris flow impacts on flexible barriers. *Int. J. Numer. Anal. Methods Geomech.* (14), 1643–1670. <https://doi.org/10.1002/nag.2806>.
- Li, X., Zhao, J., Soga, K., 2020a. A new physically based impact model for debris flow. *Geotechnique* 1–41. <https://doi.org/10.1680/jgeot.18.P.365>.
- Li, X., Zhao, J., Kwan, J.S., 2020b. Assessing debris flow impact on flexible ring net barrier: a coupled CFD-DEM study. *Comput. Geotech.* 128, 103850. <https://doi.org/10.1016/j.compgeo.2020.103850>.
- Liu, W., Yan, S., He, S., 2020a. A simple method to evaluate the performance of an intercept dam for debris-flow mitigation. *Eng. Geol.* 276, 105771. <https://doi.org/10.1016/j.enggeo.2020.105771>.
- Liu, C., Yu, Z., Zhao, S., 2020b. Quantifying the impact of a debris avalanche against a flexible barrier by coupled DEM-FEM analyses. *Landslides* 17 (1), 33–47. <https://doi.org/10.1007/s10346-019-01267-8>.
- Mergili, M., Jaboyedoff, M., Pullarello, J., Pudasaini, S.P., 2020a. Back calculation of the 2017 Piz Cengalo-Bondo landslide cascade with r.avaflow: what we can do and what we can learn. *Nat. Hazards Earth Syst. Sci.* 20, 505–520. <https://doi.org/10.5194/nhess-20-505-2020>.
- Mergili, M., Pudasaini, S.P., Emmer, A., Fischer, J.T., Cochachin, A., Frey, H., 2020b. Reconstruction of the 1941 GLOF process chain at Lake Palcacocha (Cordillera

- Blanca, Peru). *Hydrol. Earth Syst. Sci.* 24, 93–114. <https://doi.org/10.5194/hess-24-93-2020>.
- Ng, C.W.W., Song, D., Choi, C.E., Koo, R.C.H., Kwan, J.S.H., 2016. A novel flexible barrier for landslide impact in centrifuge. *Geotech. Lett.* 6 (3), 221–225. <https://doi.org/10.1680/jgele.16.00048>.
- Ng, C.W.W., Wang, C., Choi, C.E., De Silva, W.A.R.K., Poudyal, S., 2020. Effects of barrier deformability on load reduction and energy dissipation of granular flow impact. *Comput. Geotech.* 121, 103445. <https://doi.org/10.1016/j.compgeo.2020.103445>.
- Pierson, T.C., 2005. Hyperconcentrated flow-transitional process between water flow and debris flow. In: *Debris-flow Hazards and Related Phenomena*. Springer, Berlin Heidelberg, pp. 159–202. https://doi.org/10.1007/3-540-27129-5_8.
- Potyondy, D.O., Cundall, P.A., 2004. A bonded-particle model for rock. *Int. J. Rock Mech. Min. Sci.* 41 (8), 1329–1364. <https://doi.org/10.1016/j.ijrmmms.2004.09.011>.
- Pudasaini, S.P., 2012. A general two-phase debris flow model. *J. Geophys. Res. Earth Surf.* 117 (3), 1–28. <https://doi.org/10.1029/2011JF002186>.
- Pudasaini, S.P., 2019a. A full description of generalized drag in mixture mass flows. *Eng. Geol.* 265, 105429. <https://doi.org/10.1016/j.enggeo.2019.105429>.
- Pudasaini, S.P., 2019b. A fully analytical model for virtual mass force in mixture flows. *Int. J. Multiphase Flow* 113, 142–152. <https://doi.org/10.1016/j.ijmultiphaseflow.2019.01.005>.
- Pudasaini, S.P., Fischer, J.T., 2020. A mechanical model for phase separation in debris flow. *Int. J. Multiphase Flow* 129, 103292. <https://doi.org/10.1016/j.ijmultiphaseflow.2020.103292>.
- Pudasaini, S.P., Mergili, M., 2019. A Multi-phase Mass Flow Model. *J. Geophys. Res. Solid Earth* 124 (12), 2920–2942. <https://doi.org/10.1029/2019JF005204>.
- Remaitre, A., Malet, J.P., Maquaire, O., Ancey, C., Locat, J., 2005. Flow behaviour and runoff modelling of a complex debris flow in a clay-shale basin. *Earth Surf. Process Landf.* BGRG 30 (4), 479–488. <https://doi.org/10.1002/esp.1162>.
- Shan, T., Zhao, J., 2014. A coupled CFD-DEM analysis of granular flow impacting on a water reservoir. *Acta Mech.* 225 (8), 2449–2470. <https://doi.org/10.1007/s00707-014-1119-z>.
- Song, D., Ng, C.W.W., Choi, C.E., Zhou, G.G., Kwan, J.S., Koo, R.C.H., 2017. Influence of debris flow solid fraction on rigid barrier impact. *Can. Geotech. J.* 54 (10), 1421–1434. <https://doi.org/10.1139/cgj-2016-0502>.
- Song, D., Choi, C.E., Ng, C.W.W., Zhou, G.G.D., 2018. Geophysical flows impacting a flexible barrier: effects of solid-fluid interaction. *Landslides* 15 (1), 99–110. <https://doi.org/10.1007/s10346-017-0856-1>.
- Song, D., Zhou, G.G., Xu, M., Choi, C.E., Li, S., Zheng, Y., 2019. Quantitative analysis of debris-flow flexible barrier capacity from momentum and energy perspectives. *Eng. Geol.* 251, 81–92. <https://doi.org/10.1016/j.enggeo.2019.02.010>.
- Su, Y., Choi, C.E., Ng, C.W.W., Lam, H.W.K., Wong, A., Lee, C., 2020. New light-weight concrete foam to absorb debris-flow-entrained boulder impact: Large-scale pendulum modelling. *Eng. Geol.* 105724 <https://doi.org/10.1016/j.enggeo.2020.105724>.
- Su, Y., Choi, C.E., Lv, Y.R., Wang, Y., Li, X., 2021. Towards realistic simulations of the impact dynamics of boulders on rock-filled gabion: combined effects of rock shapes and their crushing strength. *Eng. Geol.* 283, 106026. <https://doi.org/10.1016/j.enggeo.2021.106026>.
- Tan, D.Y., Yin, J.H., Feng, W.Q., Qin, J.Q., Zhu, Z.H., 2018. Large-scale physical modelling study of a flexible barrier under the impact of granular flows. *Nat. Hazards Earth Syst. Sci.* 18, 2625–2640. <https://doi.org/10.5194/nhess-18-2625-2018>.
- Tan, D.Y., Yin, J.H., Feng, W.Q., Zhu, Z.H., Qin, J.Q., Chen, W.B., 2019. New Simple Method for Calculating Impact Force on Flexible Barrier Considering Partial Muddy Debris Flow Passing Through. *J. Geotech. Geoenviron.* 145 (9), 04019051. [https://doi.org/10.1061/\(ASCE\)GT.1943-5606.0002133](https://doi.org/10.1061/(ASCE)GT.1943-5606.0002133).
- Tan, D.Y., Yin, J.H., Feng, W.Q., Qin, J.Q., Zhu, Z.H., 2020. New simple method for measuring impact force on a flexible barrier from rockfall and debris flow based on large-scale flume tests. *Eng. Geol.* 279, 105881. <https://doi.org/10.1016/j.enggeo.2020.105881>.
- Wendeler, C., 2016. Debris-flow protection systems for mountain torrents: basics principles for planning and calculation of flexible barriers. In: *WSL Berichte. Swiss Federal Institute for Forest, Snow and Landscape Research WSL*.
- Wendeler, C., Volkwein, A., 2015. Laboratory tests for the optimization of mesh size for flexible debris-flow barriers. *Nat. Hazards Earth Syst. Sci.* 15 (12), 2597–2604. <https://doi.org/10.5194/nhess-15-2597-2015>.
- Wendeler, C., McArdell, B.W., Rickenmann, D., Volkwein, A., Roth, A., Denk, M., 2006. Field testing and numerical modeling of flexible debris flow barriers. In: *Proceedings of International Conference on Physical Modelling in Geotechnics, Hong Kong*.
- Wendeler, C., Volkwein, A., McArdell, B.W., Bartelt, P., 2019. Load model for designing flexible steel barriers for debris flow mitigation. *Can. Geotech. J.* 56 (6), 893–910. <https://doi.org/10.1139/cgj-2016-0157>.
- Winter, M.G., Macgregor, F., Shackman, L. (Eds.), 2009. *Scottish Road Network Landslides Study: Implementation*. Transport Scotland, p. 105.
- Xu, H., Gentilini, C., Yu, Z., Qi, X., Zhao, S., 2018. An energy allocation based design approach for flexible rockfall protection barriers. *Eng. Struct.* 173, 831–852. <https://doi.org/10.1016/j.engstruct.2018.07.018>.
- Yu, Z.X., Zhao, L., Liu, Y.P., Zhao, S.C., Xu, H., Chan, S.L., 2019. Studies on flexible rockfall barriers for failure modes, mechanisms and design strategies: a case study of Western China. *Landslides* 16 (2), 347–362. <https://doi.org/10.1007/s10346-018-1093-y>.
- Zhang, B., Huang, Y., 2021. Unsteady overflow behavior of polydisperse granular flows against closed type barrier. *Eng. Geol.* 280, 105959. <https://doi.org/10.1016/j.enggeo.2020.105959>.
- Zhao, J., Shan, T., 2013. Coupled CFD-DEM simulation of fluid-particle interaction in geomechanics. *Powder Technol.* 239, 248–258. <https://doi.org/10.1016/j.powtec.2013.02.003>.
- Zhou, Z.Y., Kuang, S.B., Chu, K.W., Yu, A.B., 2010. Discrete particle simulation of particle–fluid flow: model formulations and their applicability. *J. Fluid Mech.* 661, 482–510. <https://doi.org/10.1017/S002211201000306X>.
- Zhou, G.G., Du, J., Song, D., Choi, C.E., Hu, H.S., Jiang, C., 2020. Numerical study of granular debris flow runoff against slit dams by discrete element method. *Landslides* 17 (3), 585–595. <https://doi.org/10.1007/s10346-019-01287-4>.